Dense integration of solvent-free electrodes for Li-ion supercabattery with boosted low temperature performance

Abstract

Supercabatteries combine the advantages of high power and energy density performances. However, the electrodes are always fabricated using high surface area materials and traditional slurry coating method containing the solvent mixing and drying processes, which are less controlled, energy-intensive, and environmentally unfriendly. Herein, we report a solvent-free method in pilot stage, combining a high-speed air blowing, hot-rolling, and hot overlying process. The carbon materials with high content of 40% are mixed in the LiFePO4-activated carbons cathode and Li4Ti5O12-activated carbons anode, respectively. The compact densities of the thick solvent-free electrodes (120 μm, one-side) are almost ~1.6 times of the values for the slurry coating electrodes. The solvent-free full cells show capacitive linear charge/discharge curves before the cell voltage plateaus. And these linear curves further mitigate the internal resistance drop at −40 °C using acetonitrile-assistant carbonate-based eutectic electrolytes. The full cell delivers high areal capacity of 1.4 mAh cm−2 and volume energy density of 95 Wh L−1, which is almost 2 times higher than that of the slurry coating full cell. Moreover, the supercabattery with acetonitrile-assistant electrolyte shows excellent cycling retention of 92% for over 5000 cycles due to the self-passivated solid electrolyte interface formation and stable fibrous polytetrafluoroethylene net-like binding structure.

Graphical abstract

Image 1

Download : Download high-res image (314KB)Download : Download full-size image

Solvent-free electrodesLow-temperatureFree-standing filmsPTFE fibrationEutectic electrolytesHot-rolling

1. Introduction

With the increasingly prominent issues of environmental pollution and high energy consumption, the research and development of energy storage devices with both excellent electrochemical performance and green manufacturing process have attracted various attentions. Recently, the lithium-ion batteries (LIBs, 200–500 Wh L−1) [1] are the most widely studied energy storage devices. However, they are trapped in low specific power density (<500 W kg−1), a relatively poor cycling stability (<3000 cycles), and low-temperature fading. Unlike the sluggish redox reactions due to the kinetic hindrance of Li-ion diffusion and the structural instability caused by repeated Li-ion intercalation/deintercalation in LIBs, the

supercapacitors (SCs) relying on non-faradaic form of energy storage show a high power density of 10 kW kg−1 and the best cycling performance over 100000 cycles with wide applicable temperature range. But, it has a much lower energy density of 6–10 Wh L−1 [[2], [3], [4]]. Li-ion capacitors (LICs) are new type of energy storage devices combining the advantages of LIBs and SCs in a single form. One type of LICs is assembled by a battery-type electrode providing higher energy density than SCs and a capacitor-type electrode which provides high power density than LIBs [[5], [6], [7]]. These combined systems have attracted great attentions of academics and industry. As early as 2005, the company of Fuji Heavy Industry disclosed the manufacturing technology of LICs [8]. Plenty of lithium ions were injected in the negative electrode, while the positive electrode was commonly used activated carbon materials (ACs). Unfortunately, there was still the problem of low volumetric energy density (10–20 Wh L−1) [9]. Moreover, compared with LIBs and SCs, the additional prelithiation process in the manufacturing process of LICs, which is also a key step, inevitably encountered numerous difficulties such as the complicated operations, high cost, difficult to control, and high risk of using Li metal [10,11]. Unlike using only one kind of material in a single electrode, the supercabattery combines both SCs and LIBs electrode materials in one electrode. Hence, the supercabattery does not need the prelithiation process and deliver much higher energy density. For instance, Dubal et al. [12] proposed the concept of a double-hybridization and prepared the anode by combining the faradaic materials and the capacitor-type materials in a single electrode in series, and then it was cooperated with the capacitive cathodes in parallel. Especially, mixing the spinel Li4Ti5O12 (LTO) with ACs as anode has received extensive attention in the research of hybrid anodes [13] for the excellent cycling stability, such as a cell assembled by LTO-AC nanotubes and capacitive ACs cathode [14], or using electro-spinning process to get LTO/carbon hybrid nanofibers [15], even by a copolymerization and post-activation process to prepare LTO-ACs hybrid anode [16]. Other peers have shown the same concept regarding hybrid cathode by combining battery- and capacitor-type materials. The performances of various kinds of LiFePO4 (LFP)/AC (or CNTs) composite cathodes were also extensively investigated [[17], [18], [19], [20], [21], [22], [23]].

Yet, there are two main issues for the supercabatteries. At first, the electrode manufacturing still mainly uses the traditional slurry coating (TSC) process. Due to the use of high surface area carbonaceous materials, the TSC method always causes poor slurry stability, high binder content, high porosity, and low tap density, resulting in low volumetric energy density and poor performance uniformity. Moreover, the inherent problems of moisture, bad mechanical properties of electrode, and poor adhesion are difficult to solve for using the TSC method [24]. It is well known that the low moisture or organic solvent residues are the important guarantee for the cycling performance of EDLCs, which is also the same for the LICs or supercabattery. As early as 2004, the Maxwell company revealed a liquid-free dry electrode production process for fabricating the SCs electrode [25], which is superior to TSC process in cost, SCs-performance, and pro-environment. Recently, Shellikeri et al. [24] used a dry method to fabricate the LFP/ACs composite electrodes and cells with excellent cycling performance. However, in this process, the use of blender was difficult to efficiently achieve the homogenous PTFE fibrillation structure. Until now, quite few works have been reported on the battery-type electrode using solvent-free process, especially in large-scale way.

For the second issue, due to the battery faradaic element in the electrodes, the short board of LIBs at low temperature is also same for the supercabattery. When the temperature is below 0 °C, the energy and power are severely negatively affected [[26], [27], [28]]. Previous works show that the capacity of lithium batteries at −40 °C is reduced by 90% compared to the capacity at room temperature [[29], [30], [31], [32]]. So the further development of supercabattery also needs to solve the low temperature issue. The adoption of electrolyte with a low freezing point might be a possible way. For instance, Yoon-Gyo Cho et al. [33] proposed the use of nitriles as a co-solvent in EC-based electrolytes to depress the freezing point and enhance the LIB performances at low temperature.

In this work, to solve the issues of TSC process, we develop a solvent-free (SF) method to fabricate the supercabattery electrode in pilot stage, combining a high-speed air blowing, hot-rolling process, and hot overlying process. The ACs with high content of 40% were mixed in the LFP-ACs cathode and LTO-ACs anode, respectively. The tap densities of the SF-electrodes are as high as ~1.3 g cm−3, respectively, which are 1.6 times higher than the values for the TSC-electrodes. The LFP-ACs//LTO-ACs SF-full cell delivered a high volumetric energy density of 95 Wh L−1 and excellent cycling retention of 92% for over 5000 cycles. In order to improve the performance of SF-full cells in low temperature (-40 °C), we also provide a PC/DMC(PD)-based eutectic electrolyte containing acetonitrile (AN) to reduce the electrolyte freezing point. The supercabattery delivered an effectively improved capacity retention and stable cycle performance at both 25 and -40 °C.

2. Experimental

The commercial electrochemical active materials were used for the cathode and anode materials. The composite active electrode materials consist of 60% lithium intercalation materials and 40% carbon materials (ACs, Kuraray, YP50). The lithium intercalation cathode materials is LiFePO4 (LFP), which is supplied by Deyang Weixu Lithium-Battery Technology Co. Ltd. And the lithium intercalation anode materials is Li4Ti5O12 (LTO) provided by Anhui KEDA Platinum Platform Energy Technology Co. Ltd. It should be noted here that, for LTO anode, the carbon materials also contains 12.5% high-purity artificial graphite powder (HAG, Qingdao Tianyuanda, 99.999% purity). The HAG played a key role in improving the flexibility and lubrication of the mixed powder during the rolling process due to the high rigid of LTO particles, ensuring the high yield of LTO free-standing films. As for the LFP cathode, only ACs were used in this work. The routing of the solvent-free (SF) electrode fabrication process is shown in Fig. 1. Firstly, 91 wt% active materials (LFP or LTO with carbon materials), 1 wt% Super-P carbon black, and 8 wt% polytetrafluoroethylene powders (PTFE, DuPont™) were mixed in a mixer at low temperature (0–5 °C) for keeping the PTFE in glassy state. Otherwise, higher temperature could cause the wall sticking of PTFE, resulting in the undermixing. The total mass of the powder materials are 2 kg per batch. Then the high-speed dry air accelerated through the Lavel nozzles was used for blowing the mixed powders in a semi-enclosed stainless steel container, so that the PTFE molecular chain can be extended and opened up to form fibers. The PTFE fibers form a net-like binding structure on the surface of other powder materials getting cotton candy-like powders. The candy-like powders were collected by a gas filter and then hot-rolled twice at 180 °C to form a free-standing film using a horizontal-type roller. The initial free-standing film was hot-rolled to 300–400 μm in thickness by adjusting the double roll gap with continuous winding. Then, the film thickness was further reduced to ~120 μm by the secondary hot-

rolling. The cathode film was slightly thinner than the anode film to ensure the same mass loading per unit area (~15 mg/cm2 on one-side of the electrode). Finally, the free-standing films and the graphite-protected etched Al current collectors were combined together through the other horizontal-type hot roller at 160 °C to form the solvent-free (SF) electrodes for the supercabatteries. The graphite-protected etched Al current collectors were prepared by spaying graphite ink on the etched Al current collectors (FOILTEC), as reported in our previous work [34].

Dense integration of solvent-free electrodes for Li-ion supercabattery with boosted low temperature performance

Author links open overlay panelHaitaoZhou[a1]MenghaoLiu[a1]HongquanGao[a]DongHou[a]ChongchenYu[a]ChaoLiu[a]DongZhang[a]Jian-chunWu[a]JianhongYang[a]DeChen[b]

Show more

Add to Mendeley

Share

Cite

https://doi.org/10.1016/j.jpowsour.2020.228553Get rights and content

Highlights

- Li-ion supercabattery using $LiFePO_4$- and $Li_4Ti_5O_{12}$-based electrodes with 40% carbons.
- Solvent-free electrodes combined air blowing, hot-rolling and overlying process.
- Novel supercabattery shows high areal capacity, energy density and better cycling.
- Contribution of capacitive controlled current can reach up to 68% at high rates.
- Acetonitrile-assistant eutectic electrolytes ensured the −40 °C performance.

Abstract

Supercabatteries combine the advantages of high power and energy density performances. However, the electrodes are always fabricated using high surface area materials and traditional slurry coating method containing the solvent mixing and drying processes, which are less controlled, energy-intensive, and environmentally unfriendly. Herein, we report a solvent-free method in pilot stage, combining a high-speed air blowing, hot-rolling, and hot overlying process. The carbon materials with high content of

40% are mixed in the $LiFePO_4$-activated carbons cathode and $Li_4Ti_5O_{12}$-activated carbons anode, respectively. The compact densities of the thick solvent-free electrodes (120 µm, one-side) are almost ~1.6 times of the values for the slurry coating electrodes. The solvent-free full cells show capacitive linear charge/discharge curves before the cell voltage plateaus. And these linear curves further mitigate the internal resistance drop at −40 °C using acetonitrile-assistant carbonate-based eutectic electrolytes. The full cell delivers high areal capacity of 1.4 mAh cm^{-2} and volume energy density of 95 Wh L^{-1}, which is almost 2 times higher than that of the slurry coating full cell. Moreover, the supercabattery with acetonitrile-assistant electrolyte shows excellent cycling retention of 92% for over 5000 cycles due to the self-passivated solid electrolyte interface formation and stable fibrous polytetrafluoroethylene net-like binding structure.

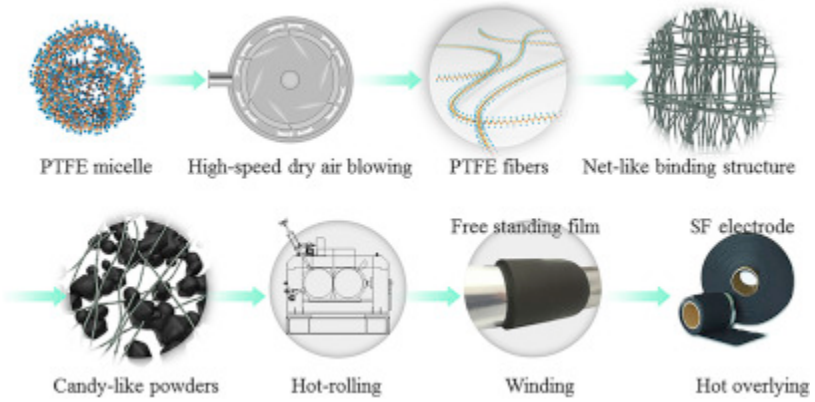

Fig. 1

Download : Download high-res image (420KB)Download : Download full-size image

Fig. 1. Schematic representation of the fabrication route for the SF-electrode.

For comparison, the traditional slurry casting (TSC) electrode was also prepared in this work. 91 wt% active material containing 60 wt% LFP cathode or LTO anode materials and 40 wt% carbon materials, were mixed with 1 wt% Super-P carbon black and 8 wt% Polyvinylidene Fluoride (PVDF, solvey™) binder in the N-methyl-2-pyrrolidone (NMP, Sigma Aldrich, anhydrous, 99.5%) solvent. The slurry was coated onto a carbon-coated Al foil current collector (20 µm, FOILTEC). The electrodes were dried in a drying oven at 80 °C and rolled through a rolling machine at room temperature to make the final TSC electrode with a total thickness of 100 µm. All the electrodes are dried in the vacuum oven at 100 °C overnight and transferred to argon-filled glove box before final cell assembly.

X-ray diffraction (XRD) analyses of the powders and free-standing films were conducted by a Bruker AXS D8 Discover diffractometer. Scanning electron microscopy (SEM) images of electrodes and powder materials were characterized by FEI Nova Nano SEM microscope.

2.1. Cell assembly and electrochemical characterization

Both the SF- and TSC-full cells were assessed with 2025 coin cells, by using cellulose film (TF4535, NKK Japan) as the separator. The electrolyte of 1 M LiPF6 PC/DMC (vol 3:1) is abbreviated as LB341 and supplied by Jiangsu Guotai Super Power New Materials Co. Ltd. For the low temperature research work, the 1 M LiPF6 acetonitrile (AN, Guotai, SCs grade) solution were added to the LB341 in the volume ratio of 0%, 15%, 30%, 50%, 65%, 80%, 95% (abbreviated as LB341, AN15, AN30, AN50, AN65, AN80, AN95), which were used for the electrolytes. Cell assembly was performed in an argon-filled glove box, in which water and oxygen concentrations were less than 0.1 ppm. For making a typical coffee-bag cell, the LTO-ACs anode, TF4535 cellulose film, and LFP-ACs cathode were punched into squares with 50 mm × 30 mm, 55 mm × 35 mm, and 50 mm × 30 mm, respectively.

Cyclic voltammetry (CV) was performed on the full cells with PARSTAT MC at scanning rates of 0.1–200 mV s−1. The EIS measurement was studied in the frequency range of 100 kHz–0.01 Hz at open circuit potential with an AC perturbation of 10 mV. The galvanostatic charge/discharge tests were performed over a voltage range of 0.1–2.7 V for full cells with an 8-channel battery analyzer (LANHE, CT3001K) at room temperature (T = 25 °C) and low temperature (T = −40 °C).The C-rates used for rate performance testing ranged from 50 mA g−1 to 1000 mA g−1.

The cycled electrodes were also characterized by SEM. This was performed by bringing the LTO-ACs SF-electrodes to a fully discharged state after full cell cycling, followed by disassembling the cell, dipping the electrode into AN (Guotai, SCs grade) solution for 10 h to remove any residual electrolyte, and finally drying at room temperature overnight inside an argon-filled glove box. X-ray photoelectron spectroscopy (XPS, Thermo ESCALAB 250XI) were carried out to analysis of the surface chemical composition of the cycled electrodes. The freezing points of the AN-assistant carbonate-based eutectic electrolytes (AN-PD (PC/DMC = 3: 1 vol%)) were measured at 5 C min−1 under nitrogen atmosphere by differential scanning calorimetry (DSC, NETZSCH, DSC200F3). All the samples were cooled down to −90 °C and then heated to a higher temperature up to 20 °C.

3. Results and discussion

3.1. Phase and morphology analysis

A schematic representation of the fabrication routing for the solvent-free (SF) electrode is shown in Fig. 1. The whole process consists of the high-speed air blowing process to fiberized the PTFE, the hot-rolling process to make the free-standing film, and hot-overlying the Al foil to fabricated the SF-electrode.

The SEM images of the LTO-ACs–SF–electrode are shown in Fig. 2a and b. The surface of the film is flat and compact. The porosity was as low as ~20%, which was measured by the Archimedes method. Compared to the TSC-electrodes with high porosity of ~40% shown in Fig. S1, the SF electrodes possess a higher compacted densities of ~1.39 g cm−3 and 1.28 g cm−3 for the LFP-AC and LTO-AC electrodes,

respectively, which are 1.6 times higher than TSC electrodes (~0.85 g cm−3). The particles with two different morphologies can be clearly observed in Fig. 2a and b. The uniformly distributed LTO subsphaeroidal particles with size of 200–500 nm tightly fill in the gap between the larger-sized ACs and HAG particles (2–5 μm), which was further demonstrated by the energy-dispersive spectral (EDS). Fig. 2b and Fig. S1b show the fibrous PTFE uniformly distributed on the surface of LTO and carbon particles to bundle them up forming a dense, integrated, and flexible net-like binding structure, which ensures the free-standing film has good mechanical stability (Fig. 3c). At the same time, the homogenously distributed inorganic particles are interconnected by fibrous PTFE, which provides critical internal small pores and facilitates the entry of the electrolyte. Moreover, the PTFE fibers with small diameter of 10–30 nm only distribute on the particle surface, instead of drilling into the pores, have negligible effect on electrode performance. Fig. 2c shows that the width-controllable LTO-ACs free-standing film with high flexibility and certain strength can be used for continuously roll-to-roll industrial production, as shown in Movie S1. Comparative X-ray diffraction (XRD) patterns of the powders, LTO-ACs, and LFP-ACs free-standing films are given in Fig. S2. For the LTO-ACs film (Fig. S2a), the main phase of the film is attributed to the LTO with typical spinel structure. Comparing to the pure LTO powder, the additional peak appearing at 26.5° is correspond to the {0 0 2} crystal plane of the HAG. However, the (101) diffraction line from PTFE was not detected at 18.1° in the film XRD pattern, which is also not observed in the XRD pattern of LFP-ACs film (Fig. S2b). Hence, the ultrafine PTFE fibers homogenously distributed in the oxides- ACs matrix and no segregation and agglomeration happened after the air blowing and hot-rolling process.

Fig. 2

Download : Download high-res image (1MB)Download : Download full-size image

Fig. 2. SEM images of the LTO-ACs–SF–electrode with (a) low magnification and (b) high magnification. (c) Width-controllable LTO-ACs free-standing film produced by a pilot line. (d) SEM image of LTO-ACs-SF electrodes from a cross-section with low magnification. (e)SEM image of LTO-ACs-SF electrodes from a cross-section at the interface between the graphite-protected etched Al current collectors and LTO-ACs film, and the corresponding EDS element mappings of C, F, Al, and Ti.

Fig. 3

Download : Download high-res image (817KB)Download : Download full-size image

Fig. 3. CV curves of the LFP-AC//LTO-AC SF-full cell between cell voltage of 0 and 2.7 V at various scan rates of 0.1–5 mV s−1 (a) and 10–200 mV s−1 (b). (c) Separation of the capacitive currents (k1v, red filled area) and diffusion currents (k2v1/2, blank area) for the SF-full cell at a scan rate of 10 mV s−1. (d) The diffusion and capacitive contribution ratio in the total intercalated charge as a function of sweep rates during CV processes. (For interpretation of the references to colour in this figure legend, the reader is referred to the Web version of this article.)

The following is the supplementary data related to this article:

Download : Download video (2MB)

Multimedia component 1.

The SEM image taken of cross-section in LTO-ACs–SF–electrodes is shown in Fig. 2d. The LTO-ACs film with uniform thickness of 120 μm stuck on the graphite-protected etched Al current collectors. And the zoomed-in picture (Fig. 2e) shows that the graphite-protected layer with thickness of 2 μm was sandwiched between the etched Al current collectors and LTO-ACs film, proving good adhesion, high conductivity, and Al protection for the anode, which guaranteed improved interface performance, as demonstrated in our previous work [34]. This sandwich structure was further verified by the corresponding EDS mapping images of the LTO-ACs-SF electrode (Fig. 3e). In addition, the uniform distribution of F element in the free-standing film also indicates the homogenously distributed fibrous PTFE, which coincides well with SEM and XRD results.

3.2. Electrochemical characterization at room temperature

Before the supercabattery performance testing works, the electrochemical mechanism and electrochemical potential window (EPW) of the LFP-AC//LTO-AC SF-full cell were determined by the cyclic voltammetry (CV) measurements. Fig. 3a and b shows the CV curves between cell voltage of 0 and 2.7 V at various scan rates of 0.1–200 mV s−1. At low scan rates of 0.1–5 mV s−1 (Fig. 3a), the CV curves display sharp cathodic and anodic peaks appearing ~2 V corresponded to the typical Li intercalation/deintercalation processes. When the scan rates increased from 10 to 200 mV s−1, the peaks broaden and were distorted to form the cathodic and anodic humps. It indicates that capacitive process affects the electrode property and combines with the faradaic process to show approximately pseudocapacitive behavior. It should be resulted from the high content of the ACs (40%) in the active materials. Yet, when the cyclic voltammetry (CV) was measured at the cell voltage of lower than 2.7 V at scan rates of 1–20 mV s−1, oxidation peaks cannot get a complete symmetrical curve, which may mean that the faradaic and non-faradaic processes of cell may cannot be utilized sufficiently. Therefore, the voltage window needs to be set above 2.7 V, but the higher voltage has no help for the improvement of performance SF-full cell, so the voltage window is set at 2.7 V. And the SF-full cell is more like a hybrid capacitor especially at high current density. Then, the faradaic reaction and capacitive contributions on the total current response were quantitatively separated, as same as the reported hybrid device works [35,36]. Fig. 3c gives the separation of the capacitive currents (red filled area, $i \propto v$) and diffusion currents (blank area, $i \propto v1/2$) for the SF-full cell at 10 mV s−1. Approximately, 33% of the total current is contributed by the capacitive-controlled process. In addition, the separations of the capacitive and diffusion contributions at other scan rates are shown in Fig. 3d. The contribution of capacitive current increased from 21% to 68% with the scan rate from 0.1 to 100 mV s−1.

The electrochemical properties of the SF- and TSC-full cells were tested by galvanostatic charge/discharge (GCD) at current densities of 0.05–1A g−1 from 0.1 to 2.7 V, which is as same as the

voltage range for commercial supercapacitor for better comparison. Hence, the developed supercabatteries (0.1–2.7 V) can be easily used for replacing the supercapacitors in some high-power applications. And the comparative rate performances are shown in Fig. 4a and b, respectively. For the SF-full cell, specific capacities of 97.3, 93.2, 86.2, 78.4, 75.3, and 65.8 mAh g−1 were obtained at increased current densities based on the total mass loadings on single electrode. The maximum areal capacity reached up to 1.4 mAh cm−2 due the thick and dense film on the SF electrode. The gravimetric capacity values are slightly higher than the ones for TSC-full cells (86.1, 81.3, 73.2, 67.8, 65.2, and 58.7 mAh g−1). Especially, the areal capacity is nearly twice as much as the value for the TSC electrode with one-side coating. But the capacity retention at high current density of 1 A g−1 was 67.7% for the SF-full cell, performing slightly lower rate capability compared to the TSC-full cell (68.1%). Especially, the larger charge/discharge plateau difference also indicates that the SF-full cell suffered kinetic issue and polarization at high current density for the SF-full cell. The improved capacity should be due to that the uniform mixing oxides and carbon particles were tightly bound by the fibrous PTFE net structure, where the interconnection and charge transfer between the particles was enhanced in the SF electrode with the higher compact density. For the TSC electrodes, some particles with poor adhesion cannot be electrochemical activated even at low current densities. However, the higher porosity of TSC electrodes was beneficial for the electrolyte penetration and performed better rate capability and low polarization. Moreover, it should be noted here that the GDC curves also show a typical battery-capacitor hybrid characteristic [24]. The capacitor-type material was initially charged/discharged in a linear curve before that the electrode potential reached the redox reaction potential of the battery-type material (Fig. 4a and b). Then, a constant battery voltage of ~1.8 V for redox reaction was succeeded by a capacitor-type curve again. This hybrid characteristic coincides well with the CV results (Fig. 2) and was further demonstrated by the electrochemical impedance spectra (EIS) measurements, as shown in Fig. 4c. The equivalent circuit for simulation of the electrochemical parameters is also given in Fig. 4c. The EIS were measured before cycling using fresh SF and TSC-full cells. Both the SF and TSC-full cells show small semicircles in the high-frequency region of Nyquist plots indicating low charge transfer resistances (Rct) [37], which are 2.9 and 3.5 Ω, respectively. In the low frequency region, the SF-full cell shows a line with an angle of 45°, resulting from a semi-infinite Warburg diffusion process [38] in the thick and compact SF-electrode, which is the typical battery characteristic followed by a capacitive 90° line. Yet, the TSC-full cell shows a line with an angle larger than 45° and quickly approaching 90° in the lower frequency region, corresponding to a transition region and finite diffusion region [38,39].

Fig. 4

Download : Download high-res image (1MB)Download : Download full-size image

Fig. 4. Comparative charge and discharge voltage profiles under different rates of (a) SF-full cell and (b) TSC-full cell. (c) Nyquist plots of SF-full cell and TSC-full cell and the equivalent circuit used to fit the experimental data. (d) Cycling stability obtained from SF-full cell and TSC-full cell at current densities of 1 A g−1. SEM images of (e) LTO-ACs-SF electrode and (f) LTO-ACs-TSC electrode after 1000 cycles.

Unlike the high tap density of SF-electrode, the TSC-electrode is relatively thinner with higher porosity gives a sufficiently short diffusion length, which causes the capacitive characteristic of TSC-full cell was

more obvious due to the quicker charge saturation [40]. But there is without the mean that TSC-full cell have no battery characteristic, and the charge and discharge voltage profiles of SF-full cell and TSC-full cell both shown a constant battery voltage of ~1.8 V for redox reaction which prove the existence of battery characteristic in TSC-full cell (Fig. 4a and b).

Long cycle life analyses were performed on the SF-full cells and TSC-full cells at current densities of 1 A g−1 and shown in Fig. 4d. Compared with the TSC-full cells, the cycling performance of SF-full cell was largely improved. For the SF-full cell, the capacity retention of 99.1% and 86.2% were registered after 2800 and 5000 cycles, respectively. And continuous capacity decay happened for the TSC-full cells. Only 33.6% of the initial capacity was maintained after 5000 cycles. The morphology of the LTO-ACs SF and TSC electrodes after 1000 cycles were examined by SEM. As shown in Fig. 4e and f, unlike the powdered surface of TSC electrodes, where the small LTO particles were detached with the large ACs particles compared to the fresh electrodes (Fig. S1), the fibrous PTFE still maintained the net-like binding structure and uniformly distributed on the compact and smooth surface of SF electrodes after 1000 cycles, which ensures the stability of the electrode material during prolonged cycling.

3.3. Electrochemical characterization at low temperature

The electrochemical performances of the SF-electrodes at low temperature were further examined by GCD at −40 °C. Acetonitrile-assistant carbonate-based eutectic electrolytes (AN-PD (PC/DMC = 3: 1 vol%)) were used for freezing point depression, as reported by Cho et al. [33]. And the SF-full cells were assembled by using the 1 M LiPF6 PD/AN (AN = 0, 15, 30, 50, 65, 80, and 95 vol%, which are abbreviated as LB34, AN15, AN30, AN50, AN65, AN80, and AN95). Fig. 5a shows the GDC curves of all the samples obtained at 50 mA g−1 and -40 °C. Unlike most of the reported low temperature battery works with high ESR values [41,42], the IR drop was mitigated by the linear capacitive region, although the linear curve was slightly distorted compared to the curve at room temperature (Fig. 4a). This linear region is beneficial for the battery management system (BMS) to gain the state of charge/discharge (SOC/SOD) of the cell more accurately just like the advantage for supercapacitor [43]. More interestingly, the full cell capacities at −40 °C increased first and then decreased as the AN content increased in the electrolyte. And the AN50 has the highest discharge capacity of 37 mAh g−1 at 50 mA g−1, which is twice as much as that of LB341 and AN95. This approximately parabolic trend was further demonstrated by the eutectic behavior of the AN-PD (PC/DMC = 3: 1 vol%) electrolytes, which were investigated by the differential scanning calorimetry (DSC) (Fig. 5b). The phase diagram of AN-PD electrolytes was built by recording endothermic peak temperatures in thermograms obtained by DSC (Fig. 5c). Nine liquid samples of the 1 M LiPF6 PD/AN (AN = 0, 15, 30, 45, 50, 65, 80, 95, 100 vol%) were cooled down to below −90 °C to get solid. With the reduction of the AN content, the upper melting points of solid-liquid mixtures decreased first from ~-45 °C (AN100). When the volume of AN accounted for 50% in the electrolyte, the eutectic temperature reached the lowest point of ~ -87 °C. Then the upper melting point temperature increased again. In accordance with DSC, we built the phase diagram of AN-PD with solidus and liquidus lines. Hence, the eutectic composition (AN50, PD/AN = 1:1 vol%) can be considered as the most optimized value that the pure liquid phase can be easily achieved, resulting in the low viscosity and high ionic conductivity, as illustrated by Cho et al. [33] The eutectic behavior of AN-PD electrolyte coincides well with the electrochemical tests, as discussed in Fig. 5a.

Fig. 5

Download : Download high-res image (1MB)Download : Download full-size image

Fig. 5. (a) Discharge voltage profiles of the SF-full cells with 1 M LiPF6 PD/AN (AN = 0, 15, 30, 50, 65, 80, and 95 vol%) electrolytes at −40 °C. (b) Eutectic behaviour of AN-PD (PC/DMC) measured by DSC. Thermograms by DSC. Endothermic heat flow is upwards. (c) Phase diagram by using temperatures of endothermic peaks of (b), the black full lines (liquids) and dotted line (solidus) reflect the trend of experimental data. The different phases are indicated by text. (d) Charge and discharge voltage profiles of SF-full cell with AN50 electrolyte under different rates at −40 °C. (e) Comparative rate capability of the SF-full cells with four different electrolytes (LB341, AN15, AN30, and AN50). (e) Cycling stability obtained from SF-full cells with four different electrolytes at current densities of 50 mA g−1 for 100 cycles at −40 °C.

More detailed GCD curves of the SF-full cell with AN50 at increased current densities of 50–1000 mA g−1 are shown in Fig. 5d. The charge/discharge plateau dribbled away and the curves gave more capacitive characteristic at high current densities. Compared the electrolytes with different AN contents (LB341, AN15, AN30, AN50), the AN50 shows a best performance in both rate performance (Fig. 5e) and specific capacity values at low temperature. Moreover, the electrolytes with AN (AN15, AN30, AN50) showed better cycling performance compared to the LB341 without AN at 50 mA g−1 and -40 °C, as shown in Fig. 5f. The capacity retention values are 94, 88, 92, and 87% after 100 cycles, respectively. Especially, all the three full cells with AN-assistant electrolytes delivered the initial Coulombic efficiencies of >80% and stabilized after 20 cycles. For the LB341, the initial Coulombic efficiency was only 69%, which approached to 99.5% after 50 cycles. This finding validates that the AN-PD electrolytes with depressed freezing point and improved ion migration also guarantee a stable supercabattery with SF-electrodes at low temperature.

3.4. Long-term cycling and volumetric Ragone plot

The long term stability of the SF-full cells with AN-PD electrolytes was further tested at high current density of 1 A g−1 and room temperature in order to evaluate the potential applications of the new electrolyte system. Fig. 6a shows that all the three samples with AN-assistant (AN15, AN30, AN50) delivered high capacity retention values of 82, 92, and 85% after 5000 cycles, respectively, which are equal or better in cycling performance than the ones without AN (LB341, Fig. 3d). The Coulombic efficiencies fluctuate a little bit (0.5%) around the value of 100%. However, it should be noted here that unlike the sample without AN (LB341) showing constant cycling curve before 2800 cycles, the AN-assistant samples show the initial gentle and steady decline of the capacity and then gradually flatten over the long-term cycling. The morphologies of the LTO-ACs SF-electrodes with and without AN-assistant after 10, 100, and 1000 cycles were examined by SEM, as listed in Fig. S3. And Fig. 6b (insert on the right side) gives three comparative morphology examples after 10 and 1000 cycles. No noticeable change was observed for all these samples. The fibrous PTFE net-like binding structures were well-preserved. Only slight coarsening and roughening of the particles was observed after 1000 cycles, which

could be due to the solid electrolyte interface (SEI) formation. And the surface chemistry was further examined by XPS. The XPS peaks were employed to deconvolute the high resolution P2p, C1s, F1s, and O1s peaks, as shown in Fig. 6b. Table S1 summarizes the results of all the XPS peaks. Unlike the reported battery works using TSC-electrodes [44], the SF-electrodes show distinct PTFE peaks at 292.2 eV in the C1s spectra and 689 eV in the F1s spectra, which are assigned to –CF2-. It indicates that the fibrous PTFE prefer to stick on the particle surface instead of drilling into the pores as other binders with solvent due to capillarity force during drying process. In addition, the relative amount of these PTFE functions and metal oxides with peak at 529.7 eV in the O1s spectra had a little decrease, and some characteristic peaks (LiF at 684.7 eV in the F1s spectra, LixPyFz at 134.5 eV in the P2p spectra) increased slightly in intensity, which could be due to the coverage of a small amount of SEI after 1000 cycles. This is consistent with the SEM observation (Fig. S3 and Fig. 6b insert), which is the possible reason for the capacity fading during long term cycling (Fig. 6a). Moreover, there is no distinct difference in the surface functions between the two kinds of electrodes with and without AN-assistant, as shown in Fig. 6b and Table S1, except that the AN-assistant the samples show higher content of LixPyFz/LixPyOFz with peak at 687.3 eV in the F1s spectra. It indicates that the AN could promote the SEI formation resulting in the initial capacity fading. Fortunately, all the surface functions content kept constant for the AN-assistant sample during the cycling (Table S1), meaning that the SEI formation was self-passivating, prevented the continuous capacity loss, and ensured the good long-term cycling performance.

Fig. 6

Download : Download high-res image (1MB)Download : Download full-size image

Fig. 6. (a) Cycling stability obtained from SF-full cells with four different electrolytes (LB341, AN15, AN30, and AN50) at current densities of 1 A g−1 for 5000 cycles at 25 °C. (b) Comparison of the P2p, C1s, F1s, and O1s deconvolutions for the three samples derived from the experimental XPS results of the 10 and 1000 cycled LTO-ACs–SF–electrodes with or without AN-assistant electrolyte, and corresponding SEM images (insert on the right side). (c) Ragone plot of volumetric energy density vs. power density for packaged LFP-AC//LTO-AC supercabattery with TSC-electrodes (the dark yellow triangles), SF-electrodes at 25 °C (the black circles), and other state-of-the-art energy storage devices. The results of the SF-full cell at −40 °C are also given (the dark blue squares). The solid dark red squares represent carbon nano-sponges (CNS)/Al Li-ion SCs (4.3 V) [34]; the solid pink regions represent the commercial lithium ion hybrid capacitor [9]; the solid stars represent LTO + AC/LMO + AC hybrid battery capacitor [48]; the gray diamond represents 30%LMO + AC/LTO hybrid battery capacitor [49]. The photographs of the “coffee-bag” cell using LTO-ACs anode, cellulose film, and LFP-ACs cathode. (For interpretation of the references to colour in this figure legend, the reader is referred to the Web version of this article.)

The volumetric energy density stored in the SF and TSC supercabatteries were estimated from the gravimetric energy density value recorded by the testing software during the discharge process. The volume factor of the electrode material was estimated in a completely packed cell with the lamination structure (Fig. 6c insert) based on the compacted density and thickness ratio of the active material [45]. For the SF electrode with high density of ~1.3 g cm−3 and high thickness ratio of 86% (Al foil 20 μm, separator 20 μm), the volume factor of SF-supercabattery was calculated to be 1.1, which is nearly twice

as much as the value for TSC-supercabattery (~0.66) and three times than the commercial supercapacitor or Li-ion capacitor (~0.35) [46]. The energy density of the completely packed cells was plotted in a Ragone plot with that of other commercial EES devices (Fig. 6c). The maximum energy density of the SF-full cell was 95 Wh L−1, estimated by the gravimetric energy density value of 83 Wh kg−1 (based on the total mass loadings of SF-electrodes). This value was almost 2 times higher than that of the TSC-full cells, 5 times of the Li-ion capacitors (10–20 Wh L−1) [9], and comparable to lead acid batteries (Fig. 6c) [47]. And the power density can reach up to 900 W L−1 and became almost one order of magnitude higher than that of lead acid batteries. Moreover, the SF-supercabattery retained 25 W L−1 at −40 °C, which was still better than that of commercial SCs measured at room temperature. Other reported supercabattery works are also given in the Ragone plot for comparison. The LFP-AC//LTO-AC SF-supercabattery showed the high specific energy and excellent cycling performance among the Li-ion hybrid system due to the high compacted density and stable fibrous PTFE net-like binding structure. Although the SF-electrode fabrication process has many advantages, such as environmental friendly, energy-efficient, and so on, it was difficult to achieve higher porosity resulting in the power density was not as good as the reported supercabattery works [48], as shown in Fig. 6c. Further engineering studies are still needed to adjusting the porosity of the SF-electrode, in order to solve the electrolyte penetration and achieve high power density.

4. Conclusions

The SF-electrodes were successfully fabricated by a facile solvent-free method in pilot stage, combining a high-speed air blowing, hot-rolling, and hot overlying process. The AC materials with high content of 40% were mixed in the LFP-AC cathode and LTO-AC anode, respectively. The compact densities of the SF-electrode can reach up to ~1.3 g cm−3, which are 1.6 times higher than the value for the slurry coating electrode. The LFP-AC//LTO-AC SF-full cell with combining the battery and capacitor characteristics was more like a hybrid capacitor, especially, at high CV scan rates. The contribution of capacitive controlled current can reach up to 68%. The GCD curve showed a linear curve before that the electrode potential reached the redox reaction potential of the battery-type material. And this linear region further eased the IR drop at low temperature of using 1 M LiPF6 AN-assistant PD (PC/DMC = 3: 1 vol%) electrolyte. The eutectic composition (AN50, PD/AN = 1:1 vol%) with depressed freezing point can be considered as the most optimized value, resulting in the highest specific capacity of 37 mAh g−1 at −40 °C. Because of the thick SF-electrodes with high compact densities, the SF-full cell deliver a high one-side areal capacity of 1.4 mAh cm−2 (97.3 mAh g−1) and high volume energy density of 95 Wh L−1. This value was almost 2 times higher than that of the TSC-full cells and comparable to lead acid batteries. Moreover, the full cell with AN-assistant electrolyte showed excellent cycling retention of 92% for over 5000 cycles due to the self-passivated SEI formation and stable fibrous PTFE net-like binding structure. However, the porosity of the SF-electrode still needs to be optimized, in order to solve the kinetic issue of the SF-supercabattery.

CRediT authorship contribution statement

Haitao Zhou: Supervision, Funding acquisition, Writing - review & editing. Menghao Liu: Data curation, Writing - original draft. Hongquan Gao: Supervision. Chongchen Yu: Data curation. Chao Liu: Validation.

Dong Zhang: Resources. Jian-chun Wu: Data curation. Jianhong Yang: Funding acquisition. De Chen: Supervision, Project administration.

Declaration of competing interest

The authors declare that they have no known competing financial interests or personal relationships that could have appeared to influence the work reported in this paper.

Acknowledgements

We acknowledge funding from National Natural Science Foundation of China (Grants 51702131, 51774151) and Natural Science Foundation of Jiangsu Provence, China (Grant SBK2017041705). This work was also supported by Institute of Green Materials and Metallurgy, Jiangsu University (Grant 5501670001, 5501670002). Dr. Haitao Zhou and Menghao Liu contributed equally to this work.

Appendix A. Supplementary data

Download all supplementary files included with this articleHelp

The following are the Supplementary data to this article:

Download : Download Word document (9MB)

Multimedia component 2.

References

[1] Y. Zhou, X. Rui, W. Sun, Z. Xu, Y. Zhou, W.J. Ng, Q. Yan, E. Fong ACS Nano, 9 (2015), pp. 4628-4635

[2] H. Wang, Y. Zhang, H. Ang, Y. Zhang, H.T. Tan, Y. Zhang, Y. Guo, J.B. Franklin, X.L. Wu, M. Srinivasan, H.J. Fan, Q. Yan Adv. Funct. Mater., 26 (2016), pp. 3082-3093

[3] C. Liu, Z. Yu, D. Neff, A. Zhamu, B.Z. Jang Nano Lett., 10 (2010), pp. 4863-4868

[4] Q. Li, X. Guo, Y. Zhang, W. Zhang, C. Ge, L. Zhao, X. Wang, H. Zhang, J. Chen, Z. Wang, L. Sun

J. Mater. Sci. Technol., 33 (2017), pp. 793-799

[5] H. Gu, Y.-E. Zhu, J. Yang, J. Wei, Z. Zhou ChemNanoMat, 2 (2016), pp. 578-587

[6] W. Zuo, R. Li, C. Zhou, Y. Li, J. Xia, J. Liu Advanced Science, 4 (2017), p. 1600539

[7] W.J. Cao, J. Shih, J.P. Zheng, T. Doung J. Power Sources, 257 (2014), pp. 388-393

[8] N. Ando, Y. Hado, K. Matsui, M. Nagai, A. Shirakami, S. Tasaki FUJI HEAVY IND LTD, JP2006286919A

(2005)

[9] H.D. Yoo, S.-D. Han, R.D. Bayliss, A.A. Gewirth, B. Genorio, N.N. Rajput, K.A. Persson, A.K. Burrell, J. Cabana ACS Appl. Mater. Interfaces, 8 (2016), pp. 30853-30862

[10] D. Sadoway J. Occup. Med., 50 (1998), pp. 24-26

[11] H. Zhou, X. Wang, D. Chen ChemSusChem, 8 (2015), pp. 2737-2744

[12] D.P. Dubal, O. Ayyad, V. Ruiz, P. Gómez-Romero Chem. Soc. Rev., 44 (2015), pp. 1777-1790

[13] T.-F. Yi, S.-Y. Yang, Y. Xie J. Mater. Chem., 3 (2015), pp. 5750-5777

[14] H.S. Choi, J.H. Im, T. Kim, J.H. Park, C.R. Park J. Mater. Chem., 22 (2012), pp. 16986-16993

[15] H.S. Choi, T. Kim, J.H. Im, C.R. Park Nanotechnology, 22 (2011), p. 405402

[16] C. Jiang, J. Zhao, H. Wu, Z. Zou, R. Huang J. Power Sources, 401 (2018), pp. 135-141

[17] N. Böckenfeld, R.S. Kühnel, S. Passerini, M. Winter, A. Balducci J. Power Sources, 196 (2011), pp. 4136-4142

[18] B. Wang RSC Adv., 3 (2013) 20024-20033-

[19] X. Hu, Y. Huai, Z. Lin, J. Suo, Z. Deng J. Electrochem. Soc., 154 (2007), pp. A1026-A1030

[20] N. Böckenfeld, T. Placke, M. Winter, S. Passerini, A. Balducci Electrochim. Acta, 76 (2012), pp. 130-136

[21] H.S. Choi, C.R. Park J. Power Sources, 259 (2014), pp. 1-14

[22] X. Li, F. Kang, X. Bai, W. Shen Electrochem. Commun., 9 (2007), pp. 663-666

[23] X.-L. Wu, Y.-G. Guo, J. Su, J.-W. Xiong, Y.-L. Zhang, L.-J. Wan Advanced Energy Materials, 3 (2013), pp. 1155-1160

[24] A. Shellikeri, S. Yturriaga, J.S. Zheng, W. Cao, M. Hagen, J.A. Read, T.R. Jow, J.P. Zheng

J. Power Sources, 392 (2018), pp. 285-295

ArticleDownload PDFView Record in Scopus

[25] P. Mitchell, X. Xi, L. Zhong, B. Zou MAXWELL TECHNOLOGIES, INC, US7492571B2 (2005)

[26] E.J. Plichta, M. Hendrickson, R. Thompson, G. Au, W.K. Behl, M.C. Smart, B.V. Ratnakumar, S. Surampudi

J. Power Sources, 94 (2001), pp. 160-162

[27] Y. Luo, X. Xu, Y. Zhang, Y. Pi, Y. Zhao, X. Tian, Q. An, Q. Wei, L. Mai Advanced Energy Materials, 4 (2014), p. 1400107

[28] C.R. Sides, C.R. Martin Adv. Mater., 17 (2005), pp. 125-128

[29] C.K. Huang, J. Sakamoto, J. Wolfenstine, S. Surampudi J. Electrochem. Soc., 147 (2000), pp. 2893-2896

[30] S.S. Zhang, K. Xu, T.R. Jow Electrochim. Acta, 48 (2002), pp. 241-246

[31] H.-P. Lin, D. Chua, M. Salomon, H. Shiao, M. Hendrickson, E. Plichta, S. Slane Electrochem. Solid State Lett., 4 (2001), pp. A71-A73

[32] G. Zhao, Z. Wei, N. Zhang, K. Sun Mater. Lett., 89 (2012), pp. 243-246

[33] Y.-G. Cho, Y.-S. Kim, D.-G. Sung, M.-S. Seo, H.-K. Song Energy Environ. Sci., 7 (2014), pp. 1737-1743

[34] H. Zhou, M. Liu, Y. Li, C. Liu, H. Gao, Z. Cao, D. Zhang, X. Jin, Q. Chen, Y. Liu, J. Yang

J. Electrochem. Soc., 165 (2018), pp. A3100-A3107

[35] I.E. Rauda, V. Augustyn, B. Dunn, S.H. Tolbert Acc. Chem. Res., 46 (2013), pp. 1113-1124

[36] H. Zhou, C. Liu, J.-C. Wu, M. Liu, D. Zhang, H. Song, X. Zhang, H. Gao, J. Yang, D. Chen

J. Mater. Chem., 7 (2019), pp. 9708-9715

[37] X. Qu, Z. Yu, D. Ruan, A. Dou, M. Su, Y. Zhou, Y. Liu, D. Chu ACS Sustain. Chem. Eng., 8 (2020), pp. 5819-5830

[38] C. Ho, I.D. Raistrick, R.A. Huggins J. Electrochem. Soc., 127 (1980), pp. 343-350

[39] H. Zhou, F. Lou, P.E. Vullum, M.-A. Einarsrud, D. Chen, F. Vullum-Bruer Nanotechnology, 24 (2013), p. 435703

[40] S. Motupally, C.C. Streinz, J.W. Weidner J. Electrochem. Soc., 142 (1995), pp. 1401-1408

[41] J. Xu, X. Wang, N. Yuan, J. Ding, S. Qin, J.M. Razal, X. Wang, S. Ge, Y. Gogotsi Energy Storage Materials, 23 (2019), pp. 383-389

[42] W. Wang, T. Yang, S. Li, W. Fan, X. Zhao, C. Fan, L. Yu, S. Zhou, X. Zuo, R. Zeng, J. Nan

Electrochim. Acta, 317 (2019), pp. 146-154

[43] L. Kouchachvili, W. Yaïci, E. Entchev J. Power Sources, 374 (2018), pp. 237-248

[44] S. Ge, Y. Leng, T. Liu, R.S. Longchamps, X.-G. Yang, Y. Gao, D. Wang, D. Wang, C.-Y. Wang

Science Advances, 6 (2020), Article eaay7633

[45] M.F. El-Kady, V. Strong, S. Dubin, R.B. Kaner Science, 335 (2012), pp. 1326-1330

[46] Y. Zhu, S. Murali, M.D. Stoller, K.J. Ganesh, W. Cai, P.J. Ferreira, A. Pirkle, R.M. Wallace, K.A. Cychosz, M. Thommes, D. Su, E.A. Stach, R.S. Ruoff Science, 332 (2011), pp. 1537-1541

[47] P. Simon, Y. Gogotsi Nat. Mater., 7 (2008), pp. 845-854

[48] D. Ruan, Y. Huang, L. Li, J. Yuan, Z. Qiao J. Alloys Compd., 695 (2017), pp. 1685-1690

[49] X. Hu, Z. Deng, J. Suo, Z. Pan J. Power Sources, 187 (2009), pp. 635-639